

## A new look at bubbles during biofilm inoculation reveals pronounced effects on growth and patterning

Farnaz Asayesh,<sup>1</sup> Mir Pouyan Zarabadi,<sup>1</sup> and Jesse Greener<sup>1,2,a)</sup>

<sup>1</sup>Département de Chimie, Faculté des Sciences et de Génie, Université Laval, Quebec City, Quebec G1V 0A6, Canada

<sup>2</sup>Centre de Recherche du CHU de Québec, 10 rue de l'Espinay, Quebec City, Quebec G1L 3L5, Canada

(Received 20 September 2017; accepted 24 November 2017; published online 13 December 2017)

Specially designed microfluidic bioflow cells were used to temporarily trap microbubbles during different inoculation stages of *Pseudomonas* sp. biofilms. Despite being eliminated many hours before biofilm appearance, templated growth could occur at former bubble positions. Bubble-templated growth was either continuous or in ring patterns, depending on the stage of inoculation when the bubbles were introduced. Templated biofilms were strongly enhanced in terms of their growth kinetics and structural homogeneity. High resolution confocal imaging showed two separate bubble-induced bacterial trapping modes, which were responsible for the altered biofilm development. It is concluded that static bubbles can be exploited for fundamental improvements to bioreactor performance, as well as open new avenues to study isolated bacteria and small colonies. *Published by AIP Publishing.* <https://doi.org/10.1063/1.5005932>

### I. INTRODUCTION

Research using microfluidics to study bacterial biofilms is accelerating due to unique advantages including the ability to implement diverse channel geometries and the ability to apply inherently laminar flow fields. These properties enable a strong reduction in the experimental footprints and the application of highly controlled shear forces at relevant time and size scales, which can enhance the accuracy of experiments and numerical models, as well as enable parallel studies.<sup>1–6</sup> In addition, well-controlled conditions can provide insights into bioreactor startup, biofilm growth kinetics, and homogeneity.<sup>7–9</sup> One typical problem involves moving bubbles, which are recognized as a major nuisance for biological studies in flow cells.<sup>10,11</sup> They can increase time to reach equilibrium flow conditions, change the chemistry of the surrounding liquid phase, and cause pressure drops and resistance to flow.<sup>12–14</sup> Of particular concern, is the enhanced wall shear stress generated as bubbles flow by surfaces, which can disrupt or modify surface-attached microorganisms and biofilms.<sup>10,11,15,16</sup> On the other hand, stationary bubbles and their effects on biological systems in flow cells are less studied, probably because they are difficult to control and observe predictably.<sup>17</sup> Nevertheless, they may be at least as important in terms of their effects on biofilm growth. For example, they can modify wall properties and local flow patterns, as well as block bulk liquid from contacting the walls.<sup>18,19</sup> In microchannels, stationary bubbles are amplified in terms of their probability of formation and their effects due to typically hydrophobic walls and high surface area to volume ratios.<sup>20,21</sup> While static bubbles can undermine the advantages of microfluidic systems to study biofilms, simultaneous control over their formation and fate opens the door to a better understanding of these effects.<sup>5,11,22,23</sup>

Here, trapped bubbles in low aspect ratio microchannels were studied in terms of their effects on the formation of biofilms from *Pseudomonas* sp. bacteria. Contrary to intuition,

<sup>a)</sup>jesse.greener@chm.ulaval.ca

surfaces which were temporarily blocked by bubbles could drastically enhance the biofilm growth rate. Moreover, the affected biofilms were patterned in shapes that matched the bubbles before they detached from the wall. With the use of optical quality microfluidic devices and high resolution confocal laser scanning microscopy (CLSM), the nature of initial interactions between the bacteria and the bubbles was revealed. The resulting changes to structural heterogeneity and local growth kinetics can have important implications for the performance of continuous flow bioreactors.<sup>24–26</sup> The findings can also open new avenues to study isolated bacteria and early biofilm formations.

## II. MATERIALS AND METHODS

### A. Inoculant preparation

In this study, we used *Pseudomonas fluorescens* CT07 (motile, gram negative, rod-shaped) tagged with a chromosomally integrated green fluorescent protein (GFP). In the literature, this bacteria is reported as *Pseudomonas* sp. strain CT07.<sup>27</sup> A pre-culture of planktonic *Pseudomonas* sp. was used as the inoculum, which was obtained by shaking the cultures of planktonic bacteria in 3 ml of 5 mM AB growth media at 300 rpm for 18 h at 30 °C. Growth media used for cultivation in the microfluidic flow cell were either modified AB or Luria-Bertani (LB) type (Sigma Aldrich, Canada). The AB medium consisted of 1.51 mM (NH<sub>4</sub>)<sub>2</sub>SO<sub>4</sub>, 3.37 mM Na<sub>2</sub>HPO<sub>4</sub>, 2.20 mM KH<sub>2</sub>PO<sub>4</sub>, 179 mM NaCl, 0.1 mM MgCl<sub>2</sub>·6H<sub>2</sub>O, 0.01 mM CaCl<sub>2</sub>·2H<sub>2</sub>O, and 0.001 mM FeCl<sub>3</sub> with 10 mM Na-citrate·6H<sub>2</sub>O as the sole carbon source. The modified LB growth stream consisted of 0.1 wt. % tryptone and 0.05 wt. % yeast extract and NaCl concentrations of 0.1 wt. % (17 mM).

### B. Microfabrication

The mold design was done by the computer aided design software (DraftSight™, Dassault systèmes, France). The mold was fabricated by adhering a laminate photoresist (SY300 film, Fortex, UK), on a 75 × 50 × 1 mm glass slide (12-550C, Fisher Scientific, Canada) using a thermal benchtop dry film laminator (FL-0304-01, Fortex, UK). The adhered photoresist was exposed to UV light through a mask using a vacuum exposure unit (AY-315, Fortex, UK) and excess photoresist was removed using developer and rinse solutions (SY300 Developer/Rinse, Fortex, UK). Figure S1 ([supplementary material](#)) shows the mold at the bottom of a Petri dish.

Microfluidic devices were made by pouring polydimethyl siloxane (PDMS) (Sylgard184, Dow Corning, Canada) and cross linker solution (10:1 ratio) against the mold and curing at 70 °C overnight. After curing, the cross-linked PDMS device was cut and peeled from the mold. Two inlets were punched at the upstream positions and one outlet at the furthest downstream position. The PDMS device was sealed by a 75 × 50 × 170 μm glass coverslip (12-548C, Fisher Scientific, Canada), which enabled a high quality optical surface for microscope-based observation. The device was placed cover slip down on an inverted microscope for imaging in transmission and CLSM (fluorescence) modes.

### C. Microchannel design and properties

Figure 1(a) shows the channel design used in this study. It included two different inlets, I<sub>1</sub> and I<sub>2</sub>, in order to apply different solutions to study the effect of bubbles during the different stages of inoculation. All liquid flowed off-chip through a single outlet, O. The channel included a “head” and “body” with widths of 2 mm, which were each separated by a “neck” with width 250 μm. The channel height was 50 μm throughout the device. The reduction in the channel width in the neck resulted in calculated increases to flow velocities by nearly 8 times. Bubble trapping was encouraged in the head and body portion due to a low aspect ratio ( $h/w = 0.025$ ) and relatively slow flow velocities, compared to the neck. Figure 1(a) insets (i and ii) show channel cross-sections in the body and neck regions. We estimated enhancement of bubble trapping by 6–10 times versus taller channels typically used in our work ( $h \geq 150 \mu\text{m}$ ). Also, bubble entrapment was enhanced by assuring the full recovery of the hydrophobic wall

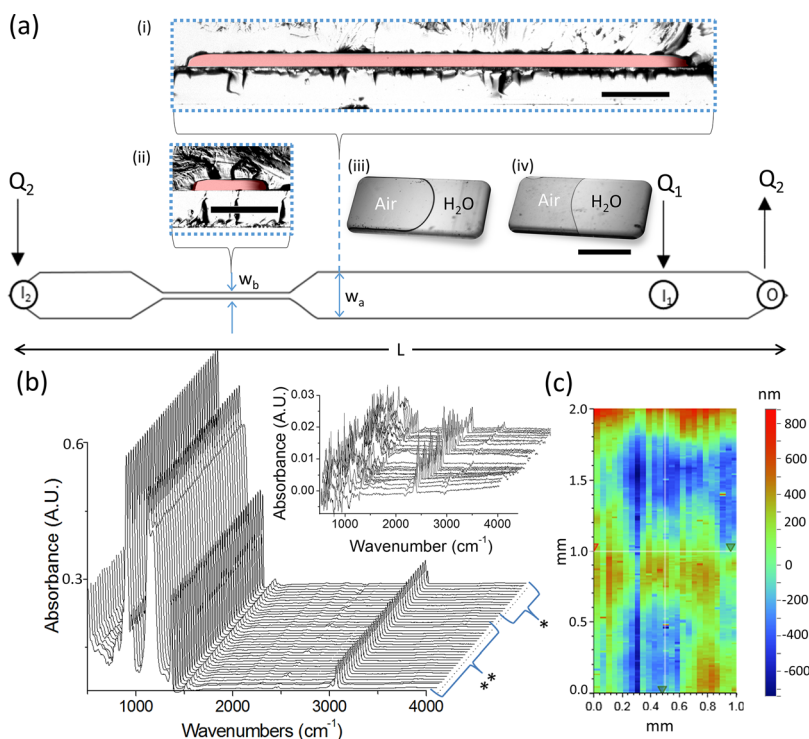


FIG. 1. (a) Schematic of the microchannel. Flow was left to right with the liquid being introduced into the device through inlets  $I_1$  and  $I_2$  with volumetric flow rates  $Q_1$  and  $Q_2$ , respectively. The liquid left the channel through the outlet,  $O$ , at a flow rate of  $Q_T = Q_1 + Q_2$ . The channel width was  $w_a = 2000 \mu\text{m}$  to  $w_b = 250 \mu\text{m}$ . Inset images (i) and (ii) show cross-sections of the channel (highlighted in red) with the glass cover slip and the PDMS channel at the lower and upper surfaces, respectively. Inset scale bars  $250 \mu\text{m}$ . The device length was  $L = 6 \text{ cm}$ . Recovery of the wall hydrophobicity is shown in the inset immediately after (iii) and 48 h after (iv) plasma bonding via the changing wall angle at the gas-liquid interface for an air plug. The scale bars are  $2 \text{ mm}$ . (b) FTIR spectra using an air background acquired along the length of the microchannel in two regions upstream (\*) and downstream (\*\*) of the neck region. The spectra were normalized to 1 based on the  $790 \text{ cm}^{-1}$  peak of approximately 0.55 absorbance units. The inset shows recalculated spectra using a PDMS background. (c) Representative image showing the surface morphology of a  $1 \times 2 \text{ mm}$  segment within the microchannel. The color bar indicates the heights for both images.

properties after sealing with plasma gas. This was confirmed by monitoring the air/liquid contact angle at the wall in time. Full hydrophobic recovery was noted after 48 h. Figure 1(a) (insets iii and iv) shows the results for hydrophobic and hydrophilic walls. To ensure that the transition to hydrophobic surface properties was complete and uniform throughout the channel, devices were dried with a continuous stream of filtered air for 30 min and then exposed to low heating ( $40^\circ\text{C}$ ) during a three day recovery period. The effect of hydrophobicity on bubble trapping was crucial. Almost no bubbles could be trapped for longer than a few minutes under flow conditions used in this study if devices were used less than 5 h after plasma bonding. More information on the effect of channel hydrophobicity on bubble trapping is given in the [supplementary material](#) (Sec. 3). Finally, the device was operated with the PDMS surface up and the glass sealing coverslip down to enhance the interaction between buoyant bubbles and their hydrophobic surfaces.

Uniformity in channel properties were verified to ensure that localized variations in biofilm growth were due to randomly trapped bubbles and not from localized chemical or topographical anomalies at the channel surface. To verify that chemical properties were uniform throughout the channel, ATR-FTIR was conducted at intervals of  $1 \text{ mm}$ , along the length of the channel. Details of the experiment and band assignments are given in the [supplementary material](#). Figure 1(b) shows the position-dependent vibrational absorbance bands (relative to an air background) from different positions along the channel. Characteristic PDMS bands were observed at  $790$ ,  $1014$ ,  $1070$ ,  $1260$ , and  $2960 \text{ cm}^{-1}$ . Differences between in-channel spectra and a separate

PDMS sample reference were generated to more easily identify any position-dependent variations. Random differences in wavenumbers  $<1000\text{ cm}^{-1}$  were due to noise, where system sensitivity was low. The main observable differences were due to  $\text{CO}_2$  absorption ( $2350\text{ cm}^{-1}$ ), which was due to slight fluctuations in purge gas conditions. Finally, the surface roughness was measured at the bottom of the microchannel. The data presented shows an RMS roughness of 265 nm and a peak to peak roughness of  $1.6\text{ }\mu\text{m}$  in a  $1 \times 2\text{ mm}$  area. These values were approximately 0.5% and 3% of the total channel height, respectively, and were representative of results throughout the entire channel.

#### D. Fluidic control

Liquids were delivered to the microfluidic device via a perfluoroalkoxy connective tubing (outer diameter 1.6 mm) (U-1148, IDEX, WA, USA) connected to  $I_1$  and  $I_2$ . The upstream side of the tubing had a threaded connector assembly (P-200x, P-658, IDEX, WA, USA) that interfaced with a 60 ml lure lock syringe (BD Scientific, NJ, USA), which was driven by pumps (PHD 2000, Harvard Apparatus, Holliston, MA, USA).

#### E. Sterilization

Teflon tubing was first filled with pure ethanol, sonicated, and then exposed to a flow of 70:30 v/v ethanol:water for 2 h at  $2\text{ ml h}^{-1}$ . The tubing was then connected to the device and sterilization ensued by flushing the device through  $I_1$  and  $I_2$  with a 70:30 v/v ethanol:water solution for 30 min at  $Q_1 = Q_2 = 1\text{ ml h}^{-1}$ . Residual ethanol solution was washed out of the system with sterile water for an additional 2 h at  $Q_1 = Q_2 = 1\text{ ml h}^{-1}$ . All solutions were made using ultrapure water with a resistivity of  $18.1\text{ M}\Omega\text{ cm}$ .

#### F. Localized inoculation and introduction of bubbles

Biofilms were grown from *Pseudomonas* sp. bacteria in a temperature-controlled room at  $22 \pm 1^\circ\text{C}$ . Direct inoculation was confined to the downstream region (between  $I_1$  and O) using an inoculum applied to  $I_1$  and a nutrient-depleted stream applied to  $I_2$ . At later times, upstream biofilm growth (between  $I_2$  and  $I_1$ ) was achieved by blocking  $I_1$  and flowing a nutrient solution into  $I_2$ . This enabled the so-called upstream inoculation, whereby planktonic bacteria emitted from the downstream biofilm could swim upstream toward the nutrient source [Fig. 1(c)]. See the [supplementary material](#) (Sec. 5) for more details. Using upstream valves attached to the tubing at either inlet, bubbles could be introduced into the pre-inoculated (downstream) region between  $I_1$  and O at any time following inoculation, or into the initially non-inoculated (upstream) region between  $I_2$  and  $I_1$ . See the [supplementary material](#) (Sec. 4) for more details about bubble formation and the use of flow rates to control the bubble properties.

### III. RESULTS AND DISCUSSION

Figure 2 shows the three classes of experiments that were conducted in this work: (1) bubbles were admitted and released before the introduction of planktonic bacteria, (2) bubbles were formed on a pre-inoculated surface, and (3) bubbles were formed on a clean surface followed by exposure to planktonic bacteria. In all cases, the bubbles were trapped randomly throughout the channel. It was noted that once a bubble became adhered to a wall, the bubble net velocity was zero. During the time in which the bubbles were stopped in the channel, all bubble edges receded slowly (ca.  $20$  to  $400\text{ }\mu\text{m h}^{-1}$ ), due to gas molecule dissolution into the liquid phase and likely through the PDMS.<sup>28</sup> Finally, under the constant shear force of the liquid, the bubbles were eventually released. This was an instantaneous procedure, with some exceptions.

#### (1) Bubbles formed and released on a clean surface in the absence of planktonic bacteria did not affect biofilm formation:

As a control experiment, we adhered and released bubbles from a clean the microchannel wall before planktonic bacteria were admitted to the channel. Inoculation and exposure to a nutrient

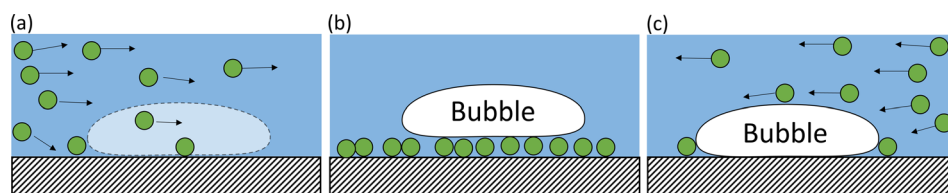


FIG. 2. (a) Planktonic bacteria (green circles) introduced to a region, where a bubble was previously attached to a sterile surface (see Sec. III (1)). (b) Bubble formed on a pre-inoculated surface (Sec. III (2)). (c) Bubble formed on a sterile surface, followed by introduction of the nutrient solution into  $I_2$  and subsequent inoculation by motile planktonic bacteria from downstream biofilms (Sec. III (3)). In all cases, the flow was from left to right.

solution followed. Biofilm formation typically occurred after a 20–40 h lag phase and no local effects from former bubbles were detected.

(2) **Bubbles formed on a pre-inoculated surface led to enhanced biofilm growth and homogeneity:**

After channel inoculation through  $I_1$  for 2 hours, a nutrient solution was admitted through  $I_1$ , marking  $t = 0$  h. In the first experiment, the bubbles were admitted to the channel immediately afterwards. The bubbles remained in place on the time scale of hours, before being washed out naturally under the force of the nutrient flow stream. The bubbles left the system as much as one and a half days before the end of a typical lag phase ended. Despite the limited interaction time between bubbles and the pre-inoculated surface, profound effects were observed on biofilm growth, many hours later. For example, Fig. 3(a) shows an irregular shaped gas bubble at  $t = 4$  h, which extended from

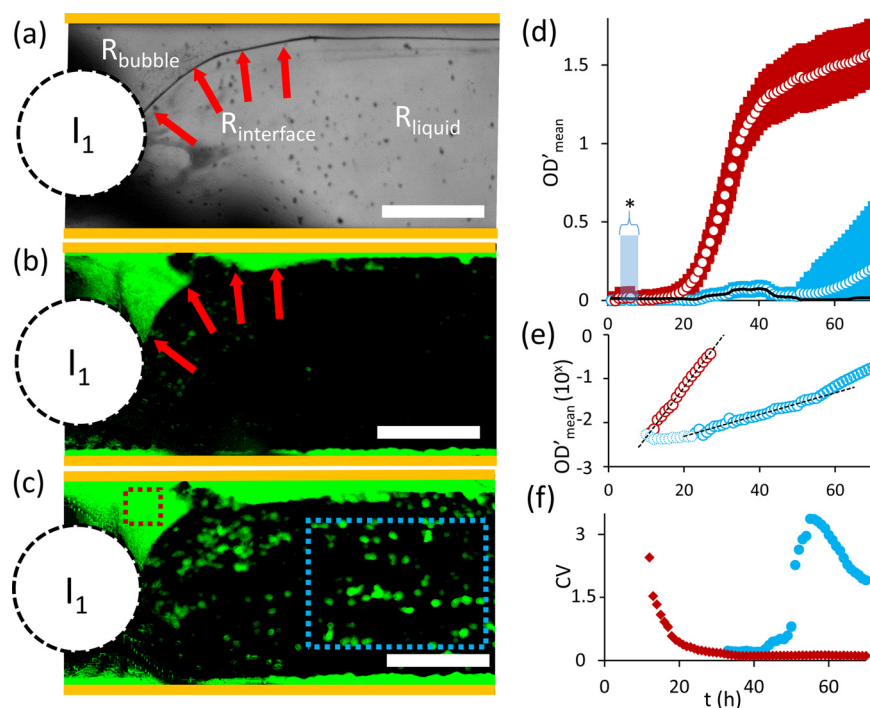


FIG. 3. (a) Transmission image at  $t = 4$  h showing a bubble in medium with the gas/liquid interface highlighted (red arrows). (b) False color OD image after 40 h showing the biofilm in the bubble region,  $R_{\text{bubble}}$ . The red arrows mark the same position as in (a). (c) OD image after 73 h, showing discrete biofilm formations in the liquid region,  $R_{\text{liquid}}$ . The red and blue boxes show, respectively, measurement locations in  $R_{\text{bubble}}$  and  $R_{\text{liquid}}$  for [(d)–(f)]. For all images [(a)–(c)], the inlet  $I_1$  is marked by a dashed circle. The scale bar is 1 mm. (d) Mean OD for biofilms in  $R_{\text{bubble}}$  (red) and  $R_{\text{liquid}}$  (blue). The error bands show standard deviation in average OD measurements. The changes to background light were measured outside of the channels (black line). The time interval in which bubbles were present is highlighted (\*). (e) Semi-log plot of mean OD after background subtraction. The dashed lines show exponential growth phases of 0.06 and  $0.26 \text{ h}^{-1}$  within  $R_{\text{liquid}}$  and  $R_{\text{bubble}}$ , respectively. (f) Structural heterogeneity, as measured by the coefficient of variance (CV). Flow rate for the nutrient solution was  $Q_1 = 0.1 \text{ ml h}^{-1}$  and for the confinement solution was  $Q_2 = 0.2 \text{ ml h}^{-1}$ .



$I_1$  to the channel sidewall. The highlighted gas/liquid interface remained in place from  $t = 0$  h and  $t = 5$  h and then was washed out rapidly. Time lapse imaging showed that biofilm growth was strongly enhanced in the region formerly occupied by the bubble ( $R_{\text{bubble}}$ ), starting at  $t = 20$  h, whereas growth in regions exposed only to liquid ( $R_{\text{liquid}}$ ) could not be detected until at least  $t = 38$  h. Figure 3(b) shows a well-formed biofilm in  $R_{\text{bubble}}$  and a barely observable one in  $R_{\text{liquid}}$  at  $t = 40$  h. At the end of the experiment, biofilm colonies were observed in  $R_{\text{liquid}}$ . The biofilm was also more homogeneous in  $R_{\text{bubble}}$  compared to  $R_{\text{liquid}}$ . To quantify differences in the lag phase, growth rate, and structural heterogeneity, time-lapse videos were analyzed for average optical density (OD) and coefficient of variance (CV) at  $R_{\text{bubble}}$  and  $R_{\text{liquid}}$ . See Sec. 2 of the [supplementary material](#) for more details on these calculations. Analysis of changes to OD in time [Fig. 3(d)] reveals that the lag phase was reduced by nearly 30 h for biofilms grown in  $R_{\text{bubble}}$  compared to those in  $R_{\text{liquid}}$ . A semi-log plot and exponential fit revealed that the initial OD doubling times ( $t_d$ ) were  $t_{d,\text{liquid}} = 11.7$  h and  $t_{d,\text{bubble}} = 2.7$  h, for biofilms in  $R_{\text{liquid}}$  and  $R_{\text{bubble}}$ , respectively [Fig. 3(e)]. Analysis of CV in time [Fig. 3(f)] shows that biofilms became more structurally homogeneous within  $R_{\text{bubble}}$  (reduced CV) during the exponential growth phase. In contrast, heterogeneity increased within  $R_{\text{liquid}}$  during the initial exponential growth phase.

In a second highlighted experiment, the bubbles were admitted through  $I_1$  at  $t = 3.5$  h. This provided more growth and development time before the bubble was introduced, compared to the situation discussed above. In this case, optical microscopy revealed the surface structure below the bubble, which is proposed to be from the early stage biofilm segments. We believe

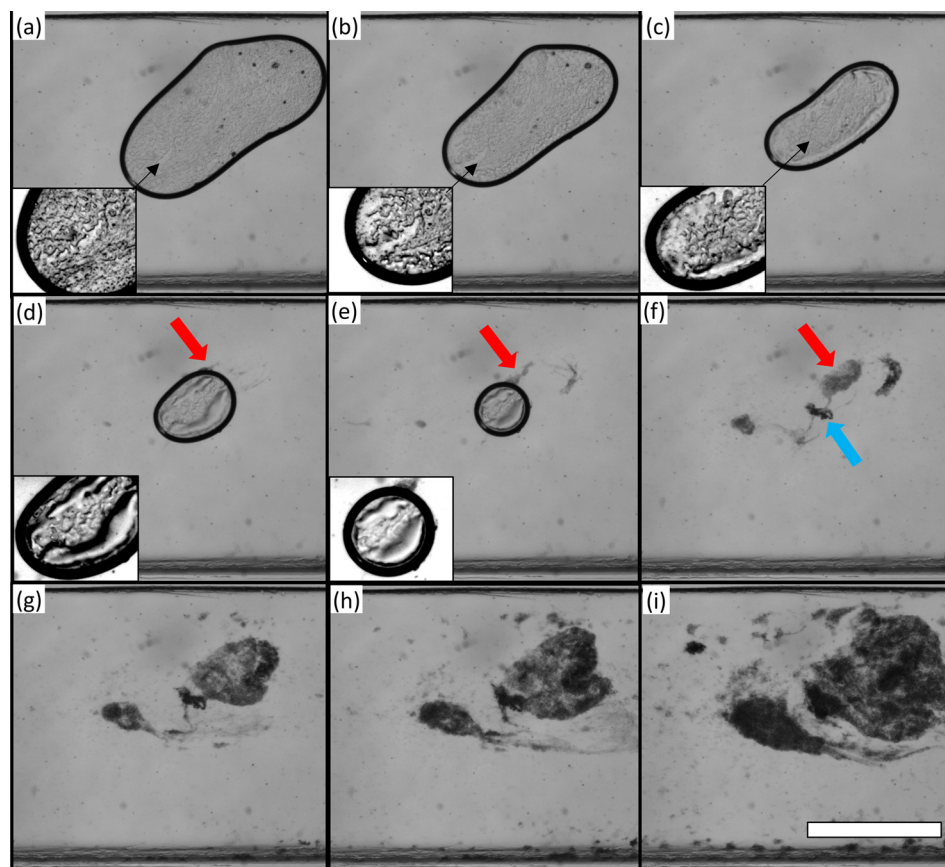


FIG. 4. A shrinking bubble on a pre-inoculated surface and restructuring of the underlying biofilm material. Images a-e show the bubble at  $t = 3.5, 6, 9.5, 12,$  and  $13$  h following a  $2$  h inoculation period. The inset figures show the zoomed areas of the bubble with contrast adjusted. The red arrows (d)–(f) show the biofilm protruding from the bubble. The blue arrow shows the residual biofilm following bubble disappearance. Frames (f)–(i) show the rapid development of the biofilm at times  $15, 16.5, 17.5,$  and  $19$  h. The scale bar in (i) is  $1$  mm.

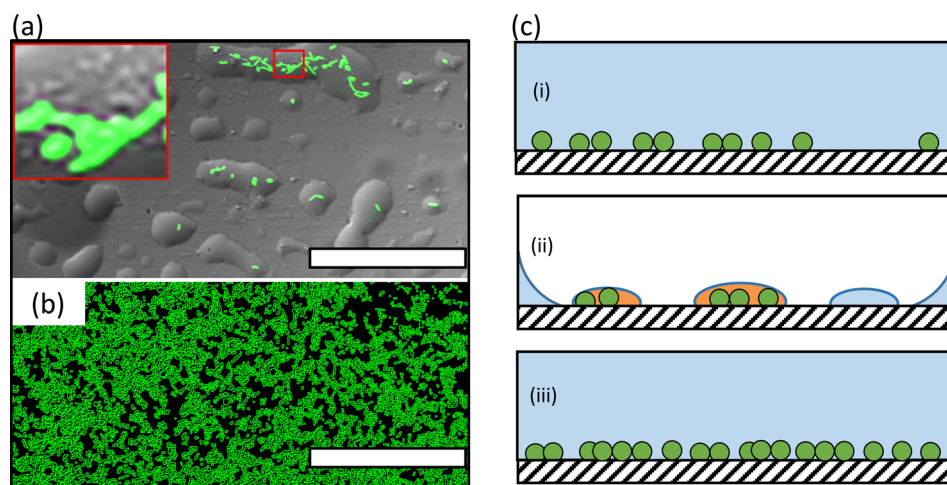


FIG. 5. (a) Superimposed images from CLSM acquired simultaneously in fluorescence and transmission modes showing trapped GFP bacteria (green) within small liquid pools (grey) on the PDMS surface. The field of view was smaller than the overall size of the air bubble. The inset shows a high contrast image showing the proposed bacterial debris, (resulting in some distortion to bright GFP bacteria). (b) Visualization of accumulated bacteria after rapid growth was observed in the same field of view as (a). The scale bars in (a) and (b) are  $80\text{ }\mu\text{m}$ . (c) A graphical depiction (cross-section perspective) of pre-inoculated bacteria on the glass surface (i), which became trapped within liquid pools under a (not to scale) large bubble (ii), followed by uniform bacterial growth throughout the region (iii). The orange colored pools indicate the proposed biochemical modifications to pools containing trapped bacteria.

that the presence of the bubble created a mismatch between the index of refraction of air and the hydrated biofilm layers at the channel surface permitting visualization in advance of obvious growth in the liquid filled channel. Figure 4 shows a relatively large bubble immediately after attachment, which then continuously shrank over the next 10.5 h. The shrinking was likely due to gas molecule dissolution into the liquid phase, or through the PDMS material, which is known to be porous to small molecules in air and liquid phases.<sup>28</sup> Shrinking caused the structured material under the bubble to become visibly displaced and reorganized, likely driven by the bubble air-liquid interface dragging across the channel surface. This may be related to the reported biofilm restructuring caused the controlled passage of bubbles against hydrophobic surfaces, but appears to be more severe.<sup>15</sup> No such observation was made with size changing bubbles atop sterile surfaces. At one point during the bubble dissolution, some biofilm could be seen to protrude into the liquid phase. After the bubble was gone, a dense biofilm deposit remained. The formerly confined biofilm segments were highly active, entering into rapid growth almost immediately after exposure to the nutrient solution. In this case, biofilm growth occurred in the approximate location of the  $R_{\text{bubble}}$ , but rapid biofilm growth quickly proceeded downstream, not appearing to be well-attached to the surface. During this time, no significant growth was observed away from the former bubble position. A supplemental time-lapse is available along with additional Figs. S12–S14 and text located in the [supplementary materials](#).

To complement time-lapse imaging, high resolution CLSM was used to investigate  $R_{\text{bubble}}$ . Figure 5(a) shows the PDMS surface while a bubble was in place, starting less than 1 h after inoculation. It can be seen that the PDMS surface was not completely dry, but instead contained residual liquid in the form of small isolated pools. Some of these pools contained bacteria that were trapped directly against the channel wall. The number of trapped bacteria varied from single isolated cells to larger groups. In some of the pools containing bacteria, non-fluorescent materials with sizes smaller than a single bacterium were observed. Similar observations were made for bubbles adhered to more mature inoculated surfaces, except that some relatively thick (ca.  $10\text{ }\mu\text{m}$ ) bacterial multi-layers could also be seen within liquid pools [[supplementary material](#), Figs. S13(a) and S13(b)]. In these cases, a large amount of non-fluorescent matter was also observed. It is believed that these were initial biofilm materials, similar to those responsible for the structured surface under the bubble in Fig. 4. Bubbles that were large enough to span the

entire vertical distance of the channel resulted in similar liquid pools and trapped bacteria on the glass slide [supplementary material, Fig. S13(c)]. However, more bacteria seemed to accumulate within larger pools on the PDMS side, indicating an expected preference for hydrophobic surfaces,<sup>15</sup> or at least a stronger ability to remain attached during disturbances associated with initial bubble adherence. It should also be considered that hydrophobic PDMS supports higher water contact angles and liquid pools under the bubble should protrude further from its surface compared to those on the glass surface, which should spread more thinly. Measurements at the channel wall, after the bubble left the pre-inoculated surface, showed a rapid and uniform accumulation of bacteria [Fig. 5(b)], which were very likely the precursor to homogeneous and optically dense biofilms previously observed in  $R_{\text{bubble}}$  [Figs. 3(b) and 3(c)]. One explanation for the enhanced growth could be related to the debris observed within some of the pools. This could have been bacterial fragments that were generated during bubble adhesion or from a triggered self-induced lysis.<sup>29</sup> The latter process has recently been noted in *Pseudomonas aeruginosa* as a mechanism that can initiate enhanced biofilm formation.<sup>29,30</sup> Similarly, accumulation of other cellular by-products within the small liquid volumes around bacteria could have simulated the biochemical environment of a more densely populated surface, thereby tricking bacteria into entering rapid growth earlier than normal.<sup>31</sup> We note that no doubling events were observed during a 5 h period for any trapped bacteria from the data series shown in Fig. 5(a). We attribute this to a rapid transition to starvation conditions within the liquid pools. This demonstrates their isolation from the bulk liquid conditions and the potential for accumulation of signaling molecules to occur. Further studies are proposed to investigate how the high bacteria to liquid volume ratios and by-product accumulation may affect bacteria behavior through modified quorum sensing or otherwise. In addition, it is proposed that that trapping bacteria within microscopic pools under bubbles of different gas types could be a novel and efficient way to study bacterial interactions and the effect of dissolved gas molecules on bacterial behavior.

### (3) Bubbles formed on clean surfaces then exposed to planktonic bacteria led to biofilm “ring patterns”:

Next, we discuss the effect of bubbles that were first formed against clean surfaces, during exposure to a nutrient-depleted liquid and were then exposed to planktonic bacteria. See the supplementary material Sec. 5 for details on the inoculation process. Figure 6 shows typical results with more examples given in the supplementary material Sec. 6. Three static bubbles can be seen trapped at  $t = 24$  h in the upstream portion of the channel, with different channel widths at each attachment point. This resulted in different average liquid velocities near bubbles 1–3 ( $v_1 = 0.3 \mu\text{m s}^{-1}$ ,  $v_2 = 0.4 \mu\text{m s}^{-1}$ , and  $v_3 = 2.1 \mu\text{m s}^{-1}$ ). During this time, a biofilm was grown downstream while a continuous flow of nutrient depleted liquid washed over the upstream region containing the bubbles. At  $t = 27$  h, the nutrient-depleted solution was replaced with a nutrient medium via  $I_2$ , which washed past the bubbles [Fig. 6(a)]. Introduction of the nutrient solution to the upstream parts of the channel enabled ejected planktonic bacteria from the downstream biofilm to follow the concentration gradient upstream and colonize the formerly sterile channel portions, between  $I_1$  and  $I_2$ . This was preferable to introducing bubbles to the clean surface via air trapped in the inoculant fluid because we could ensure that bubbles were formed on a completely clean surface. At  $t = 33$  h, 6 h after switching to the nutrient medium at  $I_2$ , the bubbles disappeared and the entire region was awash in nutrient solution [Fig. 6(b)]. At this time, the upstream portion of the channel resembled the completely empty channel at the beginning of the experiment. At  $t = 39$  h, localized biofilm growth could be seen at the former air-liquid interface region ( $R_{\text{interface}}$ ) of all three bubbles at  $t = 27$  h [Fig. 6(c)], the time when the nutrient solution was first introduced to  $I_2$ . Growth away from these positions ( $R_{\text{liquid}}$ ) was observed 5 h later and continued until the end of the experiment [Fig. 6(d)]. Optical density measurements were conducted at  $R_{\text{interface}}$  and  $R_{\text{liquid}}$ . A comparison of the OD measurements [Fig. 6(e)] revealed that the lag phase was 4 h shorter for biofilm segments at  $R_{\text{interface}}$ , compared to  $R_{\text{liquid}}$ . An analysis of the exponential growth [Fig. 6(f)] revealed a significant reduction in OD doubling time, from  $t_d = 2.6$  h ( $R_{\text{liquid}}$ ) to  $t_d = 0.99$  h ( $R_{\text{interface}}$ ). This effect was similar for all three locations, despite the



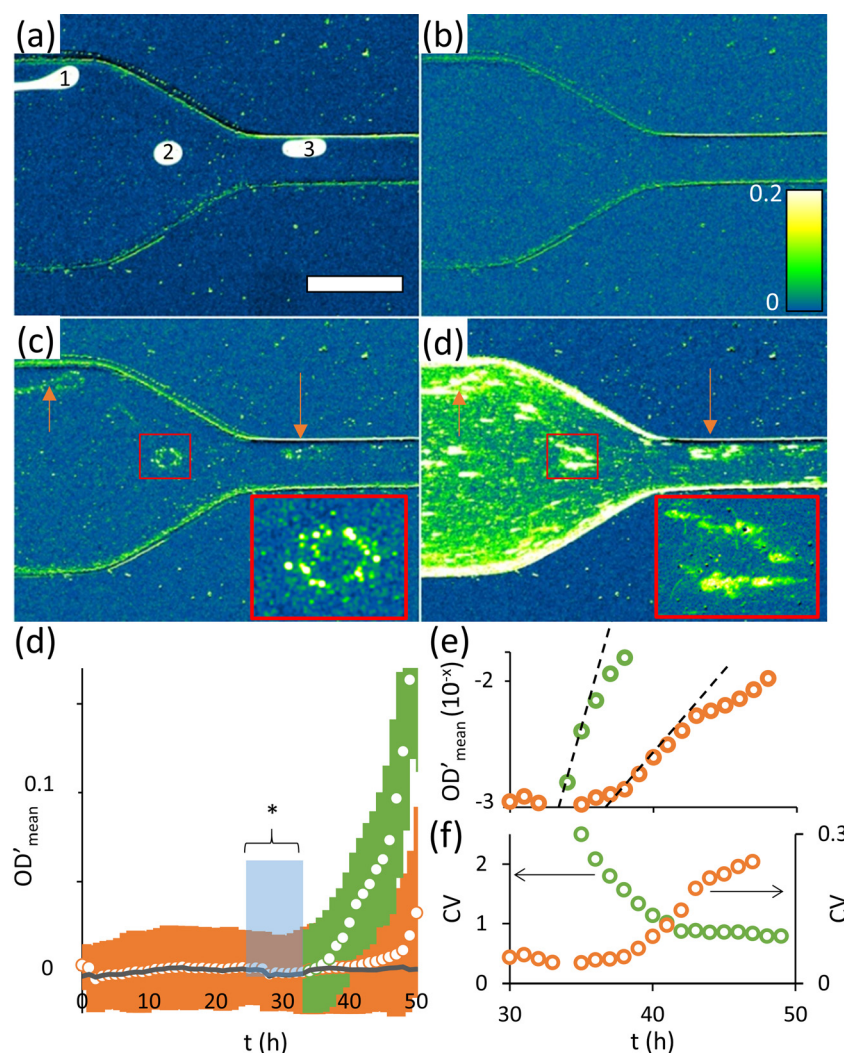


FIG. 6. (a) Bubbles (1, 2, and 3) in the nutrient solution at  $t = 27$  h after initial formation on a sterile surface under a flow or nutrient depleted solution at  $t = 24$  h. The scale bar ( $300\ \mu\text{m}$ ) is representative for (a)–(d). The flow is left to right. (b) Image at  $t = 34$  h after bubble disappearance. The color bar shows OD in (a)–(d). (c) Growth of biofilm begins at  $R_{\text{interface}}$  ( $t = 39$  h). (d) Continued growth at  $R_{\text{interface}}$  with modest growth elsewhere. The arrows in (c) and (d) point to the position of former bubbles 1 and 3. The red boxes show the zoomed images of the biofilm near  $R_{\text{interface}}$  surrounding former bubble 2 position. (e) Plot of  $OD'$  versus time for biofilms at  $R_{\text{interface}}$  (green) and  $R_{\text{liquid}}$  (orange). Color scheme is the same for (e)–(g). The error bands show standard deviation in  $OD'$  measurements. Average  $OD'$  background obtained from the outside of the channel (grey) shows background light fluctuations.  $OD'$  values were equivalent to OD after subtraction of ca. 0.02 units to account for insufficient background subtraction.  $OD'$  values for  $R_{\text{interface}}$  (green) were acquired from an average of all three bubbles. The time interval in which bubbles 1–3 were present is highlighted (\*). (f) Semi-log plot of mean  $OD'$  after background subtraction with the dashed lines showing the initial exponential growth phase with exponential growth constants  $0.06$  and  $0.26\ \text{h}^{-1}$ . (g) Structural heterogeneity, as measured by the coefficient of variance. The flow rate for the nutrient solution was  $Q_1 = 0.1\ \text{ml h}^{-1}$  through  $I_1$  and for the confinement solution was  $Q_2 = 0.2\ \text{ml h}^{-1}$  through  $I_2$ .

different bubble shapes and the local variations in flow velocity arising from differences in local channel widths and variations in bubble proximity to walls. From Fig. 6(g), it can be seen that the measured structural heterogeneity (via CV measurements) decreased significantly at the onset of rapid growth at  $R_{\text{interface}}$ , whereas it increased for during exponential growth at  $R_{\text{liquid}}$ .

The results above point to an interfacial phenomenon. Previously, micropatterned biofilms at liquid-liquid interfaces have been reported using laminar flow templating<sup>21</sup> and by micro emulsion

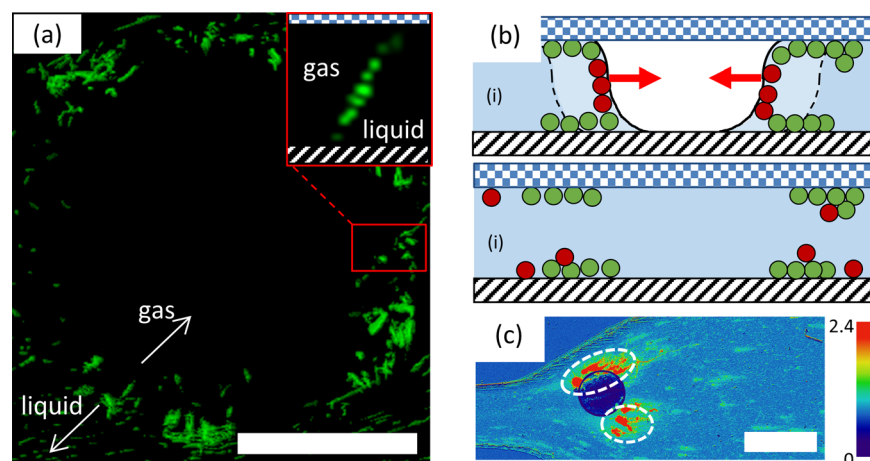


FIG. 7. (a) Top view of a volume rendered z-stack from CLSM showing bacteria surrounding a bubble which was initially attached to a clean surface. The scale bar is  $100\ \mu\text{m}$ . The inset CLSM image ( $50 \times 60\ \mu\text{m}$ ) shows a vertical cross section at the gas-liquid interface with GFP bacteria (green). The lower and upper confinement surfaces were glass (black cross-hatch) and PDMS (blue checkers), respectively. (b) The proposed mechanism for patterned surface inoculation by bacteria trapped at the air-liquid interface of a bubble initially attached to the sterile surface. (i) Controlled transfer of bacteria (green) during bubble shrinking and (ii) explosive release of bacteria at the air-liquid interface (red) during bubble collapse and release. (c) Result of the proposed explosive bacterial transfer during bubble collapse showing a double exposed OD image with the former bubble location (dark circle) and enhanced biofilm formation (highlighted with white ovals) extending in the downstream direction away from  $R_{\text{interface}}$  50 h later (with scale bar  $300\ \mu\text{m}$  and color to OD correlation given).

scaffolds.<sup>32,33</sup> No coupled enhancements to growth kinetics were reported, however. While we could find no reports of micropatterned biofilms by bubbles, it is known that some biofilm forming bacteria, including *P. fluorescens* (used here) can become physically trapped at static air-liquid interfaces.<sup>34</sup> It has also been reported that biofilm growth can proceed more quickly for some aerobic bacteria because of locally higher dissolved oxygen levels,<sup>35,36</sup> and particulate contaminants at the air-liquid interface.<sup>37</sup> While we could not find literature on bacterial accumulation at submerged bubble interfaces under flow conditions, as studied here, “shear trapping” at solid-liquid interfaces may be analogous. For example, swimming bacteria (*Escherichia coli*), monotrichous swimming bacteria (*P. aeruginosa*), and lophotrichous type swimming bacteria (*P. putida* and *P. fluorescens*) could all be trapped at interfaces due to the physics of their propulsion systems within velocity gradients near solid surfaces.<sup>38,39</sup> Other studies also showed that amphiphilic proteins and other biofilm precursor macromolecules can form robust self-assembled layers at air-liquid interfaces.<sup>40</sup>

To verify bacterial trapping at bubble interfaces in this study, we conducted CLSM measurements. We see from Fig. 7(a) that planktonic bacteria accumulated at  $R_{\text{interface}}$  in the case where bubbles were attached to a non-inoculated surface. Moreover, from z-stack images, we could see bacteria at the air-liquid and air-liquid-solid interfaces around the bubble periphery, but not in  $R_{\text{bubble}}$ . We postulate that accumulation of bacteria at  $R_{\text{interface}}$  was a combination of trapping of planktonic bacteria which were ejected from other locations and subsequent growth. The  $R_{\text{bubble}}$  region, on the contrary, was protected and no enhanced growth was observed after bubble detachment. Figure 7(b) depicts the proposed inoculation mechanism, which includes bacteria directly attached to the air-liquid interface and the three-phase air-liquid-wall interface. We do not rule out the possibility that EPS could also have begun to accumulate there as well. The same figure also illustrates a proposed mechanism for bacterial transfer from the air-liquid interface to the channel wall via a slow, continuous deposition process during bubble contraction, followed by a final collapse, marking bubble disappearance. The latter mechanism explains some observations of enhanced biofilm growth at locations that were close, but not directly adjacent, to  $R_{\text{interface}}$  which appeared to radiate from the former bubble wall in the downstream direction [Fig. 7(c)]. We note that recently published work demonstrates similar observations of bacterial patterning from a reverse system comprised of bacteria-laden droplets drying on structured surfaces.<sup>41</sup>

#### IV. CONCLUSIONS

Using microfluidic flow cells, we observed a profound relation between the presence of static, wall-adhered bubbles and enhanced growth kinetics and patterning of biofilms from *Pseudomonas* sp. bacteria. As the effect revealed itself many hours after bubbles had detached from the microchannel surface, their role in influencing biofilm development has likely gone unnoticed until now. Time-lapse movies and high resolution imaging revealed two separate mechanisms for the accumulation of bacteria. In the first, bubbles formed on clean surfaces led to bacterial trapping at the bubble periphery. This led to biofilm ring patterns. In the second, bubbles formed on pre-inoculated surfaces, resulted in trapped bacteria in small liquid pools beneath the bubble. In this case, growth enhancements could have resulted from the increased interaction between bacteria. Each mechanism led to local enhancements of growth rate and local structural homogeneity, in the vicinity of the former bubbles. Overall, however, bubbles resulted in structurally and kinetically inhomogeneous biofilms, when accounting for the average properties throughout the microchannel. This study points to important implications for biofilm flow cell users. First, it is important to account for bubbles at all growth stages; even temporarily trapped bubbles that wash out during the earliest stages of inoculation can have pronounced effects on the flow cell startup and performance. Second, trapped gas, air or otherwise, could be exploited as an easy route to grow biofilms with controllable properties, such as customizable structure and activity. Finally, we believe that the use of bubbles in microchannels can be a powerful approach to study isolated bacteria, small colonies, and early biofilms in small pools, thereby enabling control over their interactions and the environment around them.

#### SUPPLEMENTARY MATERIAL

See [supplementary material](#) for definitions of bubble regions  $R_{\text{bubble}}$ ,  $R_{\text{interface}}$ , and  $R_{\text{liquid}}$ ; equipment and experimental methodology; details on bubble formation and control over bubble properties; a supplemental image gallery showing other examples of bubble influenced growth; supplementary references; and two time lapse videos of dynamic bubbles atop pre-inoculated surfaces.

#### ACKNOWLEDGMENTS

Authors thank Otini Kroukamp for discussions about bacteria behaviour at interfaces, Cezar Khursigara about cell fate in confined environments, Milad Abolhasani and Mohammad Seyed Taghavi for discussions about hydrodynamics in the vicinity of liquid-bubble interfaces, Pascale Chevallier for microchannel profilometry and Andrée-Anne Guay-Bégin for help conducting ATR-FTIR. Greener is the recipient of an early researcher award from the Fonds de Recherche du Québec—Nature et Technologies. This research was supported by funding through the Natural Sciences and Engineering Research Council and instrumentation funded by the Canadian Foundation for Innovation.

- <sup>1</sup>J. Greener, M. Parvinzadeh Gashti, A. Eslami, M. P. Zarabadi, and S. Taghavi, *Biomicrofluidics* **10**(6), 064107 (2016).
- <sup>2</sup>A. Karimi, D. Karig, A. Kumar, and A. Ardekani, *Lab Chip* **15**(1), 23–42 (2015).
- <sup>3</sup>M. Hassanpourfard, R. Ghosh, T. Thundat, and A. Kumar, *Lab Chip* **16**(21), 4091–4096 (2016).
- <sup>4</sup>K. Drescher, Y. Shen, B. L. Bassler, and H. A. Stone, *Proc. Natl. Acad. Sci.* **110**(11), 4345–4350 (2013).
- <sup>5</sup>J. El-Ali, P. K. Sorger, and K. F. Jensen, *Nature* **442**(7101), 403 (2006).
- <sup>6</sup>M. Parvinzadeh Gashti, J. Asselin, J. Barbeau, D. Boudreau, and J. Greener, *Lab Chip* **16**, 1412–1419 (2016).
- <sup>7</sup>W. Zhang, T. S. Sileika, C. Chen, Y. Liu, J. Lee, and A. I. Packman, *Biotechnol. Bioeng.* **108**(11), 2571–2582 (2011).
- <sup>8</sup>N. B. Aznaveh, M. Safdar, G. Wolfaardt, and J. Greener, *Lab Chip* **14**(15), 2666–2672 (2014).
- <sup>9</sup>J. L. Song, K. H. Au, K. T. Huynh, and A. I. Packman, *Biotechnol. Bioeng.* **111**(3), 597–607 (2014).
- <sup>10</sup>P. K. Sharma, M. J. Gibcus, H. C. van der Mei, and H. J. Busscher, *Appl. Environ. Microbiol.* **71**(7), 3668–3673 (2005).
- <sup>11</sup>S. A. Cruz, R. Popat, M. T. Rybtke, M. Cámara, M. Givskov, T. Tolker-Nielsen, S. P. Diggle, and P. Williams, *Biofouling* **28**(8), 835–842 (2012).
- <sup>12</sup>G. Lestari, M. Alizadehgiashi, M. Abolhasani, and E. Kumacheva, *ACS Sustainable Chem. Eng.* **5**(5), 4304–4310 (2017).
- <sup>13</sup>T. Cubaud and C.-M. Ho, *Phys. Fluids* **16**(12), 4575–4585 (2004).
- <sup>14</sup>M. J. Fuerstman, A. Lai, M. E. Thurlow, S. S. Shevkoplyas, H. A. Stone, and G. M. Whitesides, *Lab Chip* **7**(11), 1479–1489 (2007).
- <sup>15</sup>H. Jang, R. Rusconi, and R. Stocker, *NPJ Biofilms Microbiomes* **3**(1), 6 (2017).

- <sup>16</sup>S. Khodaparast, M. K. Kim, J. E. Silpe, and H. A. Stone, *Environ. Sci. Technol.* **51**(3), 1340–1347 (2017).
- <sup>17</sup>Y. Kawano, C. Otsuka, J. Sanzo, C. Higgins, T. Nirei, T. Schilling, and T. Ishikawa, *PLoS One* **10**(3), e0116925 (2015).
- <sup>18</sup>E. Karatay, A. S. Haase, C. W. Visser, C. Sun, D. Lohse, P. A. Tsai, and R. G. Lammertink, *Proc. Natl. Acad. Sci.* **110**(21), 8422–8426 (2013).
- <sup>19</sup>K. Khoshmanesh, A. Almansouri, H. Albloushi, P. Yi, R. Soffe, and K. Kalantar-Zadeh, *Sci. Rep.* **5**, 9942 (2015).
- <sup>20</sup>D. Rabaud, P. Thibault, J.-P. Raven, O. Hugon, E. Lacot, and P. Marmottant, *Phys. Fluids* **23**(4), 042003 (2011).
- <sup>21</sup>D. D. Meng, J. Kim, and C.-J. Kim, *J. Micromech. Microeng.* **16**(2), 419 (2006).
- <sup>22</sup>G. Lestari, M. Abolhasani, D. Bennett, P. Chase, A. Günther, and E. Kumacheva, *J. Am. Chem. Soc.* **136**(34), 11972–11979 (2014).
- <sup>23</sup>C. Martinez, *Bubble Sci. Eng. Technol.* **1**(1–2), 40–52 (2009).
- <sup>24</sup>A. Gjaltema, P. Arts, M. Van Loosdrecht, J. G. Kuenen, and J. Heijnen, *Biotechnol. Bioeng.* **44**(2), 194–204 (1994).
- <sup>25</sup>C. Li, M. Wagner, S. Lackner, and H. Horn, *Biotechnol. Bioeng.* **113**(5), 989–1000 (2016).
- <sup>26</sup>W. G. Characklis, “Laboratory biofilm reactors,” in *Biofilms*, edited by W. G. Characklis and K. C. Marshall (Wiley, New York, 1990), pp. 55–89.
- <sup>27</sup>G. Wolfaardt, M. Hendry, T. Birkham, A. Bressel, M. Gardner, A. Sousa, D. Korber, and M. Pilaski, *Biotechnol. Bioeng.* **100**(1), 141–149 (2008).
- <sup>28</sup>G. C. Randall and P. S. Doyle, *Proc. Natl. Acad. Sci. U.S.A.* **102**(31), 10813–10818 (2005).
- <sup>29</sup>L. Turnbull, M. Toyofuku, A. L. Hynen *et al.*, *Nat. Commun.* **7**, 11220 (2016).
- <sup>30</sup>C. Schwechheimer and M. J. Kuehn, *Nat. Rev.* **13**, 605–619 (2015).
- <sup>31</sup>S. T. Flickinger, M. F. Copeland, E. M. Downes, A. T. Braasch, H. H. Tuson, Y.-J. Eun, and D. B. Weibel, *J. Am. Chem. Soc.* **133**(15), 5966–5975 (2011).
- <sup>32</sup>P. Wongkongkatep, K. Manopwisedjaroen, P. Tiposoth, S. Archakunakorn, T. Pongtharangkul, M. Suphantharika, K. Honda, I. Hamachi, and J. Wongkongkatep, *Langmuir* **28**(13), 5729–5736 (2012).
- <sup>33</sup>C. B. Chang, J. N. Wilking, S. H. Kim, H. C. Shum, and D. A. Weitz, *Small* **11**(32), 3954–3961 (2015).
- <sup>34</sup>R. Di Leonardo, D. Dell’Arciprete, L. Angelani, and V. Iebba, *Phys. Rev. Lett.* **106**(3), 038101 (2011).
- <sup>35</sup>A. Koza, P. D. Hallett, C. D. Moon, and A. J. Spiers, *Microbiology* **155**(5), 1397–1406 (2009).
- <sup>36</sup>Y. N. Chabane, S. Marti, C. Rihouey, S. Alexandre, J. Hardouin, O. Lesouhaitier, J. Vila, J. B. Kaplan, T. Jouenne, and E. Dé, *PLoS One* **9**(10), e111660 (2014).
- <sup>37</sup>Z. Zhang and G. Christopher, *Langmuir* **32**(11), 2724–2730 (2016).
- <sup>38</sup>E. Lauga, W. R. DiLuzio, G. M. Whitesides, and H. A. Stone, *Biophys. J.* **90**(2), 400–412 (2006).
- <sup>39</sup>M. Theves, J. Taktikos, V. Zaburdaev, H. Stark, and C. Beta, *Biophys. J.* **105**(8), 1915–1924 (2013).
- <sup>40</sup>W. Liu, S. Li, Z. Wang, E. C. Yan, and R. M. Leblanc, *Langmuir* **33**(30), 7548–7555 (2017).
- <sup>41</sup>A. Susarrey-Arce, A. Marin, A. Massey, A. Oknianska, Y. Díaz-Fernandez, J. Hernández-Sánchez, E. Griffiths, J. G. Gardeniers, J. H. Snoeijer, and D. Lohse, *Langmuir* **32**(28), 7159–7169 (2016).